frontiers | Frontiers in Earth Science

ORIGINAL RESEARCH
published: 26 April 2022
doi: 10.3389/feart.2022.875237

Rapid Exhumation Processes of the Gaoligong Mountain Range in the Southeastern Margin of the Qinghai–Tibet Plateau Since the Late Cenozoic

Jialong Wang[1,2], *Ni Li*[1]*, *F. M. Stuart*[3], *L. D. Nicola*[3], *Huiping Zhang*[4], *Ying Wang*[4], *Jianzhang Pang*[4] *and Yongwei Zhao*[1]

[1]Jilin Changbaishan Volcano National Observation and Research Station, Institute of Geology, China Earthquake Administration (CEA), Beijing, China, [2]The First Monitoring and Application Center, China Earthquake Administration, Tianjin, China, [3]Isotope Geosciences Unit, SUERC, East Kilbride, United Kingdom, [4]State Key Laboratory of Earthquake Dynamics, Institute of Geology, China Earthquake Administration, Beijing, China

Three continent-scale ductile shear zones trending N-S are distributed in the southeast margin of the Qinghai–Tibet Plateau. Their tectonic deformation and exhumation histories are of great significance to understanding the orogenic processes within the continent and the growth as well as expansion mechanism of the plateau. The Gaoligong shear zone (GLGSZ) is the westernmost zone near the boundary of the Indian subduction plate and is less well studied than the Ailaoshan–Red River shear zone (ASRRSZ) in the east. In this study, low-temperature thermochronological methods including apatite (U-Th)/He (AHe), zircon (U-Th)/He (ZHe), and apatite fission track (AFT) were used to date the vertical profile samples from the Gaoligong Mountain to understand the exhumation processes that occurred in the late Cenozoic. Our results show that the GLGSZ has experienced two stages of rapid exhumation events since the late Cenozoic: in the middle Miocene (~14.5 Ma) and early Pleistocene (~2.9 Ma). Based on our data, we divided the late Cenozoic tectonic deformation and exhumation processes in the Gaoligong Mountain area into two stages: 1) From the middle to the late Miocene, large-scale regional dextral strike-slip movements and lateral compressions controlled the ductile shear zone and continuously denuded the mountain surface; 2) in the Pleistocene, rapid river erosion and undercutting caused by fluctuations of the monsoon system, together with the continuous activity of brittle faults, drove the latest rapid exhumations. A comparison of the thermochronological data of the different areas along the Gaoligong Mountain shows that the exhumation rate in its northern transect is significantly higher and the time of the onset of exhumation is earlier than that in the southern transect. These results indicate that the deformation processes began in the north and continued southwards and controlled the geomorphological characteristics of the Gaoligong Mountain, whose elevation is higher in the northern part than in the southern part.

Keywords: southeastern tibet, gaoligong ductile shear zone, low-temperature thermochronology, exhumation, geomorphological evolution

OPEN ACCESS

Edited by:
Chong Xu,
National Institute of Natural Hazards, China

Reviewed by:
Honghua Lu,
East China Normal University, China
Pitsanupong Kanjanapayont,
Chulalongkorn University, Thailand

***Correspondence:**
Ni Li
lini67@sina.com

Specialty section:
This article was submitted to Structural Geology and Tectonics, a section of the journal Frontiers in Earth Science

Received: *14 February 2022*
Accepted: *29 March 2022*
Published: *26 April 2022*

Citation:
Wang J, Li N, Stuart FM, Nicola LD, Zhang H, Wang Y, Pang J and Zhao Y (2022) Rapid Exhumation Processes of the Gaoligong Mountain Range in the Southeastern Margin of the Qinghai–Tibet Plateau Since the Late Cenozoic. Front. Earth Sci. 10:875237. doi: 10.3389/feart.2022.875237

INTRODUCTION

The collision between the Indian plate and the Eurasian plate in the Cenozoic era shortened the crust of the Asian continent by approximately 2,000–2,500 km (Dewey et al., 1989; Yin and Harrison, 2000). This created the Qinghai–Tibet Plateau, the largest and highest plateau in the world, and led to extensive intracontinental deformations in the Eurasian plate (Dewey et al., 1989; Yin and Harrison, 2000). With the uplift of the Qinghai–Tibet Plateau, the plateau materials have been continuously pushed towards the southeast, and the southeast edge of the plateau forms a landform slope with high north and low south (Clark and Royden, 2000; Liu-Zeng et al., 2008). The boundary between the Indian plate and the Eurasian plate is also the most complicated active structure causing geomorphic features of the southeastern expansion and growth of the plateau. Therefore, the Qinghai–Tibet Plateau has both thrust faults and large strike-slip faults that are oblique to the boundary of the plateau, and it is difficult to explain all observed phenomena using a single continental dynamic model. Currently, the time, velocity, and mode of migration of plateau materials to the southeast are still under debate. The hypotheses on the tectonic deformation and uplift mechanism in the southeastern margin are: 1) The lower crustal flow model that emphasises consistent plateau height and continuous deformation (Royden et al., 1997; Clark and Royden, 2000); 2) extrusion along large strike-slip faults or large shear zones as the main mechanism proposed by the continental escape model (Molnar and Tapponnier, 1978; Tapponnier et al., 1982, 2001); 3) based on the brittle block model (England and Molnar, 1990), Wang et al. (2012) suggested that the outward expansion of the plateau materials occurred in the middle and late Miocene (~10 Ma), which was caused by the delamination of the lithosphere at the bottom of the plateau and the equilibrium rebound caused by it. Wang et al. (2018) quantitatively analysed the longitudinal profile of the Nu River and considered that the accelerated river cutting and rapid rock exhumation due to the climate change in the late Miocene was of great significance to the tectonic and geomorphological evolution of the southeastern margin of the plateau. Liu et al. (2009) believed that this area was mainly dominated by tectonic uplift in the Neogene, whereas erosion dominated in the Quaternary.

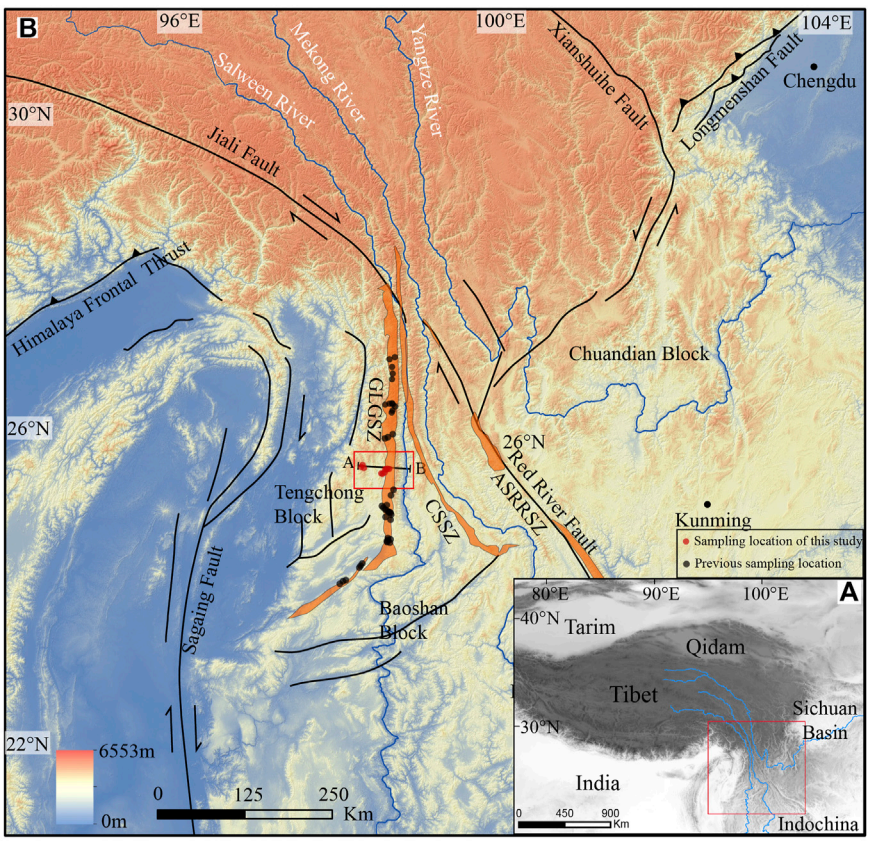

FIGURE 1 | Tectonics and regional topography of the Three Rivers Region and surrounding areas. **(A)** Simplified tectonic framework of the Tibetan Plateau. Modified from Deng et al. (2014). **(B)** Digital elevation model (DEM) of the topography and active faults in the Three Rivers Region, showing the study area (red rectangle) and sample locations in this study (red circles). DEM data is based on ~90 m Shuttle Radar Topography Mission (SRTM). Previous thermochronological ages marked by dark circles are also shown (Akciz, 2004; Wang et al., 2008; Lin et al., 2009; Song et al., 2010; Zhang et al., 2012; Liu et al., 2015; Xu et al., 2015; Tang et al., 2016; Zhang et al., 2017; Wang et al., 2018; Tang et al., 2020). GLGSZ: The Gaoligong shear zone; CSSZ: Chongshan shear zone; ASRRSZ: Ailaoshan–Red River sheer zone. Red square is the study area shown in **Figure 2**.

The Gaoligong Mountain shear zone (GLGSZ), Chongshan shear zone (CSSZ), and the Ailaoshan–Red River shear zone (ASRRSZ) are large-scale strike-slip fault zones with typical structural features that extend for thousands of kilometres across the southeastern margin of the Qinghai–Tibet Plateau (Allen et al., 1984; Clark et al., 2005, 2006; Royden et al., 2008; Wang et al., 2018; Wang et al., 2020; Shen et al., 2021; **Figure 1**). The GLGSZ is a large-scale structural zone in the southern transect of the Bangong Lake–Nu River suture zone, which was formed by the southward extrusion of blocks in the southeastern margin of the Qinghai–Tibet Plateau and consists of large-scale strike-slip faults between the blocks. The orogenic process and geomorphic evolution of these continental-scale shear zones are of great significance for revealing the deformation mechanism of the Indo-Asian Cenozoic collision inside the Asian continent (Houseman and England, 1993; Wang et al., 1998; Tapponnier et al., 2001; Liu-Zeng et al., 2008, 2018). Little research has been conducted on the GLGSZ, which is located in southwest Yunnan, owing to its relatively difficult natural environment; therefore, studies have mainly focused on geometry, kinematics, petrography, and geochronology (Ji et al., 2000; Akciz, 2004; Zhang et al., 2010; Zhang et al., 2012). Research on the exhumation, uplift, and tectonic geomorphological evolution of the GLGSZ has only started recently (Liu-Zeng et al., 2018; Liu-Zeng et al., 2018; Wang et al., 2018, 2020; Dong et al., 2021; Shen et al., 2021). These studies provide information regarding the orogenic process of the Gaoligong Mountain (Glotzbach et al., 2011).to identify the southeast migration pattern of materials in the Qinghai–Tibet Plateau and the deformation pattern of the crust in the southeast margin.

In addition, the three largest rivers in Asia, namely, the Salween River, Mekong River, and Yangtze River, originate in the Qinghai–Tibet Plateau, and flow through the nearest part of the southeast edge of the plateau by only a few tens of kilometres apart and are parallel to each other, cutting through the bedrock canyon landform of approximately 3 km (Clark et al., 2005; Liu-Zeng et al., 2008; Yang et al., 2015). Distinct geomorphic features such as high mountains and deep valleys manifest at the uplift of the Cenozoic Indo-Asian collision plateau in the southeast margin. Currently, there is little research on the timing of the geomorphic processes and on whether the erosion and undercutting process of rivers must contribute to the rapid exhumation of the large-scale structural zone in the southeastern margin of the Qinghai-Tibet Plateau. From this perspective, this study provides a quantitative assessment of the thermal history of the GLGSZ through low-temperature thermochronology. *In situ* samples of fresh gneiss and granite were collected in the transects of the Gaoligong Mountain, Guyong Rock Mass, and Yinghuagu Valley. Apatite (U-Th)/He (AHe) and zircon (U-Th)/He (ZHe) and apatite fission track (AFT) were performed, and an age-elevation vertical transect was established. A discussion on the exhumation and uplift process of the Gaoligong mountain range is provided based on the newly acquired low-temperature chronology data to outline the tectonic deformation history and landform formation of the southeast margin of the Qinghai–Tibet Plateau.

GEOLOGICAL SETTING

There are three tectonic subzones in the study area: the Gaoligong Mountain metamorphic complex belt, Tengchong Block, and Baoshan Block (**Figure 1**). The Gaoligong Group is distributed from Jiali Fault in the north to Sagaing Fault in the south, and its east and west sides are bounded by major faults manifested as the Salween River and Longchuan River, respectively. Petrological facies containing high-grade metamorphic rocks in the inner belt, which tend to be shallower from the middle to both sides, are alternately observed. Rock types are complex, including biotite plagioclase granulite, plagioclase amphibolite, eyeball-shaped striped migmatite, mixed gneiss, marble, and quartzite. Migmatization is so strong that it is impossible to distinguish between the sequences. Inner faults are extremely developed, dynamic metamorphism is strong, and tectonized rocks (fault breccia and mylonite) are common. Well-developed strata with large thicknesses are observed in the Baoshan Block, and they are distributed on both sides of the Nu River Valley and Longling–Luxi area to the east of the Gaoligong Mountain. Overall, the Baoshan Block is characterised by clastic rock, carbonate and dolomite deposits of shallow sea, coastal, and lagoon facies, and volcanic deposits. After the Jurassic period, the marine history ended and turned into continental deposits with parallel unconformity contact relationship among all systems. The stratigraphic characteristics of the Tengchong Block differ considerably from those of the Baoshan Block, with underdeveloped strata and low thickness, and the main body is coastal clastic rock deposits. The Palaeozoic strata are primarily of Silurian, Devonian, and Carboniferous origin, the Mesozoic strata are only of Triassic origin, and the Cenozoic volcanic rocks are particularly developed. This indicates that the Tengchong Block has been a terrestrial environment for a long time.

Since the Cenozoic, strike-slip faults have been the most developed tectonic structure in the study area and its surroundings. Among them, the Nabang strike-slip zone (Najman et al., 2020) on the western edge is a dextral strike-slip fault of the same scale and nature as that of the Gaoligong strike-slip zone. Dextral strike-slip faults of different scales and levels are also exposed between the two fault zones. Gaoligong strike-slip fault zone extends to the east Himalayan tectonic section in the north, turns to the south *via* Fugong and Lushui to Longling, and turns to the south *via* Ruili to the Sagaing fault in the west, with a total width of approximately 8–12 km. Gaoligong strike-slip zone in the north of Longling is distributed in the north-south direction, while in the west it turns to the north-east direction. Its altitude exceeds 3 km, and its elevation gradually decreases from north to south. It is also the watershed between the Longchuan River in the west and the Nu River in the east, and it divides the Baoshan Block and the Tengchong Block. The mountain is mainly composed of high-grade metamorphic rocks and granite (Zhong et al., 1991; Wang et al., 1998). The east of the shear zone consists of shallow metamorphic rocks of the Palaeozoic Gongyanghe Group, in which fold cleavage and cataclastic structures are developed. The deep mylonite of the Paleoproterozoic Gaoligong Mountain

Group is exposed to the west, which is composed of granite mylonite, various light-coloured veins, cataclastic rocks, and mylonite. The deformation of the mountain is strong. The Gaoligong strike-slip zone consists mainly of a dextral strike-slip as evidenced by combining the lineation and foliation of the shear zone (Socquet and Pubellier, 2005; Tang et al., 2016). Under the action of near east–west compressional shear, the right-lateral strike-slip GLGSZ was bent and connected with the Sagaing fault, and since the Miocene, the compression of the Indian plate to the Eurasian plate intensified (Yang et al., 2006, 2011). According to the results measured by the K-Ar method of muscovite and Ar/Ar method of amphibolite and biotite, it is estimated that the ductile strike-slip deformation age of Gaoligong is 32–22 Ma (Ji et al., 2000; Wang et al., 2006). The quaternary GLGSZ sides are mainly characterised by the strike-slip movement of brittle faults. In the southern section, some normal faults are observed, forming a series of graben and semi-graben basins (Wang et al., 2008), which may be related to the formation of a series of NE-trending faults in the region. The frequent earthquake events in this area in modern times (An et al., 2009. Chang et al., 2011) indicate that the faults in this area are still active. The Nabang strike-slip fault zone, which starts from the vicinity of Xima-Tongbiguan in the east and reaches the east side of the Cenozoic basin in Myanmar in the west, is an integral part of Myanmar's Magu belt (Mitchell, 1993), and is characterised by dextral strike-slip and thrust faults. The main periods of activity are 24–19 Ma and 14–11 Ma (Ji et al., 2000). The Gaoligong fault zone constitutes an important structural transformation zone for block extrusion and uplift in the southeast margin of the Qinghai–Tibet Plateau. Three large rivers in Asia, namely, the Salween, Mekong, and Yangtze Rivers, flow south along the southeast margin of the plateau, shaping deep canyon landform. In this Three Rivers region, there are many studies about evolution, bed rock profile, and clastic rocks of the river. (Ouimet et al., 2010; Yang et al., 2015; Shen et al., 2021).

SAMPLING AND METHOD

Sampling Strategy

Low-temperature thermochronology is a quantitative study of the thermal history of rocks. Information regarding the cooling process of the upper crust can be obtained by the time–temperature relationships of minerals. The geological applications of low-temperature thermochronology include absolute dating of rocks and tectonic processes, exhumation history of various geological backgrounds, long-term geomorphological evolution process, and basin analysis. AHe, fission track (FT), and ZHe are the most widely used low-temperature thermal chronological methods, and their closure temperatures ranges are 60–80°C, 100–120°C, and 180–200°C, respectively. Assuming that the paleogeothermal gradient is ~30°C/km, they record the exhumation process of rocks passing through ~6 km of the upper crust by low-temperature thermal chronological methods (Farley, 2000; Reiners, 2005; Guenthner et al., 2013). Therefore, we used low-temperature thermal chronological age data of 10 samples collected from the Gaoligong vertical transect (GLG), Guyong rock transect (GY), and Yinghuagu transect (YHG) to discuss the exhumation history of the Gaoligong Mountain by simulating the time-age process (**Figure 2**). The lithology of the shear zone mainly comprises gneiss and granite. Four samples were collected in the vertical transect of the Gaoligong Mountain, and the collection route was from Linjiapuzi in the west of the Gaoligong Mountain to Shangshan Road in the Nanzhai Public House with a horizontal distance of approximately 5 km and an elevation difference of 945 m (from 2,210 to 3,164 m, 20TC08-20TC11). No large-scale brittle fault transect was found in the geological map or in the field.

U-Th/He Analysis

At first, we tested the ages of AHe and ZHe for the above samples. Three to five mineral grains were analysed for each sample. There may be some differences between the ages of each grains, which may be related to the differences in crystal sizes (Reiners and Farley, 2001), the influence of zircon zonation (Ault and Flowers, 2012), radiation damage (Flowers et al., 2009), and experimental conditions. The AFT age was determined by laser ablation inductively coupled plasma mass spectrometry (LA-ICPMS) to directly determine the concentration of single particle ^{238}U in the sample, and then calculate the age of the sample by combining it with the spontaneous track density. Errors in the calculated spontaneous track density caused by the small number of tracks in the tested sample might exist and affect the accuracy of the estimated age. We analysed 10 samples using the Ahe method. Apatite grains were separated using the conventional heavy liquid method. Automorphic crystal grains with complete shape and no visible impurities were selected under a polarizing microscope. Only those crystal grains with a length and width of >60 μM were considered suitable for (U-Th)/He dating. Each mineral grain was wrapped in a 1 mm × 1 mm platinum bag and placed in a laser cavity. ^{4}He was degassed at 800–1000°C, and its abundance was measured using a quadrupole mass spectrometer. After degassing, the mineral particles were dissolved in concentrated HNO_3, and then the U-Th-Sm concentration of each dissolved particle was measured using mass spectrometry. Each particle was corrected by FT (Farley, 2002) to obtain the best age estimate. The error in age is caused by the analytical uncertainty of He, U, Th, and Sm measurements and the variance in the age of a single grain.

In the GLG transect, the ages of AHe were measured in the range of 3.6–4.4 Ma (**Figure 2**, **Figure 3**, **Table 1**). The ages of ZHe were in the range of 4.7–5.9 Ma (**Table 2**). Changes in age values at different elevations of the same transect may be affected by an active fault. The estimated ages of all standard samples used in the experiment are within the error range of international reports. The ages of AHe and ZHe are mostly young, and we found that there is no significant correlation between the single grain age and eU, which means that radiation damage has little effect on age. Both AHe and Zhe age-elevation maps show a steep positive correlation, which indicates that the rock mass cooled rapidly at this stage. Three samples were collected in Guyong (GY) and Yinghua Valley (YHG) transects and analysed by AHe. GY transect samples TCFT03, TCFT07, and TCFT08 were

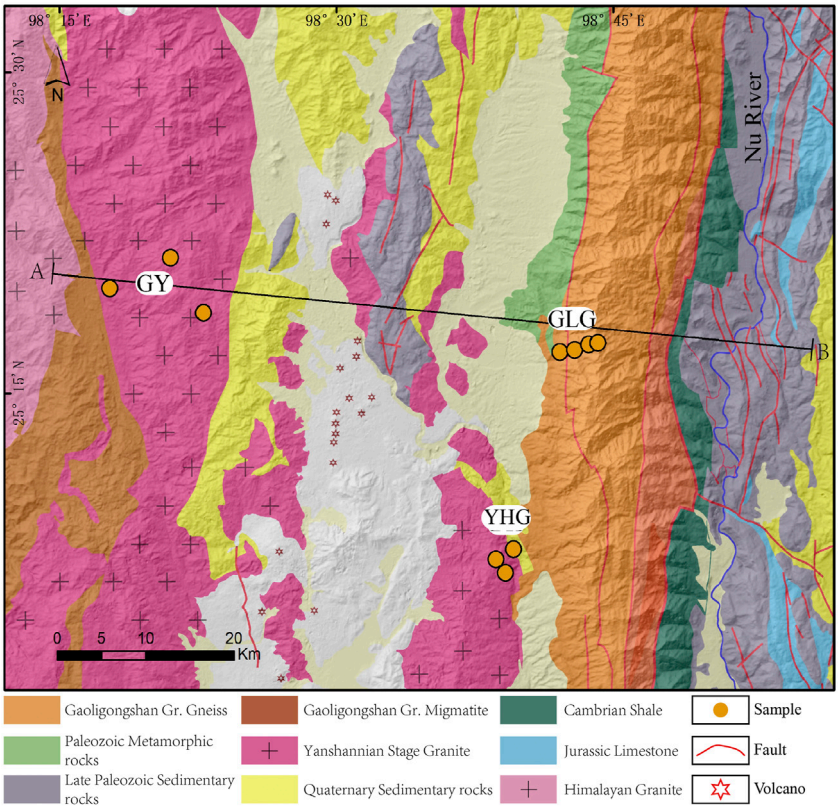

FIGURE 2 | Simplified geological map superimposed on shaded relief of the Tengchong area. Locations of samples collected for this study are shown.

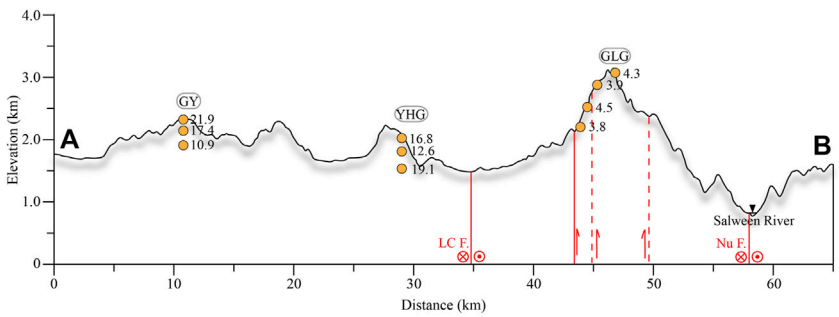

FIGURE 3 | Topographic cross section of Tengchong area **(Figure 1**: **A,B)**. The numbers in the figure represent the ages of AHe. GY, Guyong transect; YHG, Yinghua Valley transect; GLG, Gaoligong transect; Nu F, Nujiang fault; LC F, Longchuangjiang fault.

collected at elevations of 1,760 m, 2,273 m, and 2,147 m and indicate ages of 10.9 ± 0.8 Ma, 21.9 ± 4.3 Ma, and 17.4 ± 1.7 Ma (**Figure 3**) (**Table 3**), respectively. YHG profile samples 19 TC 05, 19 TC 04, and 19 TC 03 were collected at elevations of 1,430 m, 1,744 m, and 2,052 m and indicate ages of 19.1 ± 16.4 Ma, 12.6 ± 1.0 Ma, and 16.8 ± 1.6 Ma (**Figure 3**) (**Table 3**), respectively. We abandoned two estimates that had significant errors (**Tables 1**, **3**). Generally, the age of vertical profile samples increases gradually with the increase in elevation, or the change is small and concentrated in a certain time scale. The relationship between the elevation above sea level and the age estimate based on low-temperature chronology represents the average exhumation rate of this time scale. In this study, by combining AHe and ZHe age data of the GLG transect, the long-term exhumation rate was estimated using the relationship between age and elevation (**Figure 4**). The average ages of AHe and ZHe in this transect are closely related to altitude (**Figure 4**), and therefore the least square method was used to fit

TABLE 1 | Results of the apatite single particle (U-Th)/He analysis in the Gaoligong ductile shear zone (GLGSZ).

Sample ID	U (ppm)	Th (ppm)	He (ppm)	eU (mol)	Length (μM)	Width (μM)	FT	Cor date (Ma)	±σ (Ma)	Mean date (Ma)	±σ (Ma)	Latitude	Longitude	Elevation (m)	Rock type
20TC08-1	10.35	22.21	4.08E–03	1.08E–13	148.4	91.1	0.69			3.63	1.09	25.284	98.703	2,210	gneiss
20TC08-2	4.68	7.84	4.92E–04	1.30E–13	197.5	107.7	0.79	4.40	0.10						
20TC08-3	5.07	23.34	3.73E–04	8.55E–14	162.5	81.8	0.70	2.34	0.07						
20TC08-4	4.07	8.33	3.02E–04	1.02E–13	170.9	106.6	0.74	3.13	0.09						
20TC08-5	23.55	33.81	2.41E–03	4.78E–13	193.4	118.1	0.76	4.67	0.08						
20TC09-1	20.04	18.18	1.35E–03	1.07E–13	113.6	66.5	0.62	4.18	0.10	4.52	0.30	25.286	98.716	2,590	gneiss
20TC09-2	15.51	18.89	1.18E–03	8.17E–14	109.9	65.7	0.61	4.49	0.12						
20TC09-3	18.32	64.82	2.14E–03	1.03E–13	130.4	55.5	0.60	4.92	0.10						
20TC09-4	64.14	39.65	4.91E–03	3.62E–13	120.3	68.8	0.69	4.49	0.07						
20TC09-5	0.04	0.23	3.51E–01	2.42E–16	127.3	54.6	0.53	50,181.83	2,393.56						
20TC10-1	49.31	32.51	3.76E–03	1.11E–12	205.9	104.2	0.75	4.06	0.06	4.03	0.30	25.29	98.728	2,805	Granite
20TC10-2	38.46	18.90	2.60E–03	4.07E–13	169.6	98.4	0.72	3.89	0.06						
20TC10-3	30.25	15.48	1.90E–03	3.09E–13	164.5	79.8	0.69	3.78	0.07						
20TC10-4	43.61	31.42	2.96E–03	8.99E–13	205.0	80.1	0.69	3.89	0.05						
20TC10-5	39.11	44.48	3.37E–03	8.31E–13	175.0	77.5	0.69	4.54	0.06						
20TC11-1	35.74	44.36	2.84E–03	3.42E–13	163.6	72.3	0.66	4.34	0.07	4.42	0.43	25.291	98.737	3164	Granite
20TC11-4	31.15	29.33	2.29E–03	2.18E–13	138.9	68.8	0.69	4.04	0.07						
20TC11-5	30.36	22.83	2.44E–03	1.96E–13	111.8	75.3	0.65	4.88	0.08						

eU: effective uranium concentration, a parameter that weights the decay of the two parents for their alpha productivity, by (U) + 0.235 × (Th) (Flowers et al., 2009). FT is the alpha-ejection correction after Farley et al. (1996). Errors on the (U-Th)/He dates (1σ) are based on analytical uncertainty in U,Th, and He measurements. Standard deviation for the replicate analyses. Dates that were excluded from the mean calculation.

TABLE 2 | Results of the zircon single particle (U-Th)/He analysis in the Gaoligong ductile shear zone (GLGSZ).

Sample ID	U (ppm)	Th (ppm)	He (ppm)	eU (mol)	Length (μM)	Width (μM)	FT	Cor date (Ma)	±σ (Ma)	Mean date (Ma)	±σ (Ma)	Latitude	Longitude	Elevation (m)	Rock type
20TC08-1	426.30	57.92	4.44E–02	1.81E–11	254.5	107.8	0.83	5.66	0.12	5.99	0.63	25.284	98.703	2,210	gneiss
20TC08-2	779.67	118.62	9.21E–02	2.51E–11	226.6	98.9	0.81	6.52	0.15						
20TC08-3	118.36	40.80	1.24E–02	7.00E–12	304.5	109.6	0.84	5.40	0.11						
20TC08-4	419.75	60.68	4.15E–02	1.01E–11	202.8	89.2	0.80	5.58	0.13						
20TC08-5	149.59	84.77	2.00E–02	5.32E–12	251.0	88.0	0.80	6.81	0.14						
20TC09-1	479.74	83.00	5.54E–02	5.27E–12	159.6	79.5	0.73	7.02	0.15	5.67	1.05	25.286	98.716	2590	gneiss
20TC09-2	298.60	127.71	2.28E–02	5.47E–12	169.0	87.5	0.78	4.14	0.09						
20TC09-3	152.46	52.50	1.57E–02	3.38E–12	191.7	98.5	0.79	5.64	0.13						
20TC09-4	157.85	153.13	1.99E–02	4.03EV12	203.1	87.8	0.78	6.10	0.12						
20TC09-5	163.33	104.28	1.76E–02	4.39E–12	186.2	108.0	0.80	5.45	0.11						
20TC10-1	353.75	282.55	3.14E–02	9.82E–12	216.9	87.6	0.79	4.40	0.09	4.7	0.31	25.29	98.728	2805	Granite
20TC10-2	475.16	418.41	4.39E–02	6.58E–12	157.9	82.8	0.74	4.81	0.09						
20TC10-3	207.34	149.77	2.15E–02	8.37E–12	253.5	103.2	0.81	5.08	0.10						
20TC10-5	512.54	420.11	4.04E–02	3.43E–12	117.2	72.1	0.68	4.50	0.09						
20TC11-1	447.23	403.74	5.54E–02	1.01E–11	196.3	86.8	0.77	6.13	0.13	5.98	0.36	25.291	98.737	3164	Granite
20TC11-2	507.04	338.81	5.75E–02	8.48E–12	184.9	79.4	0.75	6.04	0.12						
20TC11-3	404.44	250.18	4.30E–02	1.23E–11	237.5	93.7	0.79	5.44	0.11						
20TC11-4	427.71	371.01	5.05E–02	1.02E–11	202.9	78.5	0.78	5.86	0.12						
20TC11-5	693.55	435.46	8.57E–02	1.49E–11	189.9	83.2	0.78	6.43	0.13						

eU: effective uranium concentration, a parameter that weights the decay of the two parents for their alpha productivity, by (U) + 0.235 × (Th) (Flowers et al., 2009). bFT is the alpha-ejection correction after Farley et al. (1996). cErrors on the (U-Th)/He dates (1σ) are based on analytical uncertainty in U, Th, and He measurements. Standard deviation for the replicate analyse.

TABLE 3 | Results of the apatite single particle (U-Th)/He analysis in the GY and YHG transects.

Sample ID	U (ng)	Th (ng)	He (cc)	Width (μM)	Length (μM)	Raw date (Ma)	FT	Cor date (Ma)	±σ (Ma)	Mean date (Ma)	±σ (Ma)	Latitude	Longitude	Elevation (m)	Rock type
TCFT03-1	0.11	0.59	2.50E−10	90	260	8.2	0.73	11.20	0.20	10.93	0.83	25.332	98.297	1760	Granite
TCFT03-2	0.14	0.88	3.64E−10	100	240	8.7	0.75	11.60	0.20						
TCFT03-3	0.07	0.53	1.54E−10	90	180	6.6	0.66	10.00	0.20						
TCFT07-1	0.06	0.06	2.70E−10	110	190	32.0	0.75	42.70	1.40	21.95	4.31	25.365	98.351	2,273	Granite
TCFT07-2	0.01	0.12	6.70E−11	90	130	13.3	0.70	18.90	0.50						
TCFT07-3	0.02	0.18	1.30E−10	80	130	16.6	0.67	25.00	0.60						
TCFT08-1	0.01	0.17	8.60E−11	90	180	13.3	0.72	18.60	0.40	17.40	1.70	25.314	98.381	2,147	Granite
TCFT08-2	0.01	0.00	-8.70E−12	60	150	11.5	0.60	19.20	-8.2						
TCFT08-3	0.08	0.60	3.70E−10	200	230	13.8	0.85	16.20	0.30						
19TC03-1	0.14	2.06	8.46E−10	70	150	11.1	0.68	16.50	0.40	16.80	1.67	25.123	98.645	2052	Granite
19TC03-2	0.06	3.19	1.12E−09	70	130	11.5	0.68	16.80	2.80						
19TC03-3	0.02	1.68	6.30E−10	80	150	12.5	0.65	19.30	1.00						
19TC03-4	0.18	2.10	7.78E−10	70	150	9.5	0.65	14.60	0.30						
19TC03-5	0.17	1.25	5.67E−10	70	150	10.1	0.60	16.80	0.30						
19TC04-1	0.09	0.79	2.21E−10	50	140	6.6	0.54	12.20	0.20	12.63	1.02	25.112	98.654	1744	Granite
19TC04-2	0.23	1.66	5.49E−10	65	120	7.3	0.62	11.90	0.20						
19TC04-3	0.06	0.56	1.73E−10	50	120	7.3	0.53	13.80	0.20						
19TC05-1	0.03	0.23	1.55E−10	60	110	14.8	0.59	25.20	0.50	19.10	16.42	25.13	98.66	1430	Gneiss
19TC05-2	0.02	0.16	1.28E−10	60	100	18.3	0.58	31.60	0.70						
19TC05-3	0.03	0.23	2.83E−12	60	120	0.3	0.59	0.50	0.00						

FT is the alpha-ejection correction after Farley et al. (1996). Errors on the (U-Th)/He dates (1σ) are based on analytical uncertainty in U,Th, and He measurements. Standard deviation for the replicate analyses. Dates that were excluded from the mean calculation.

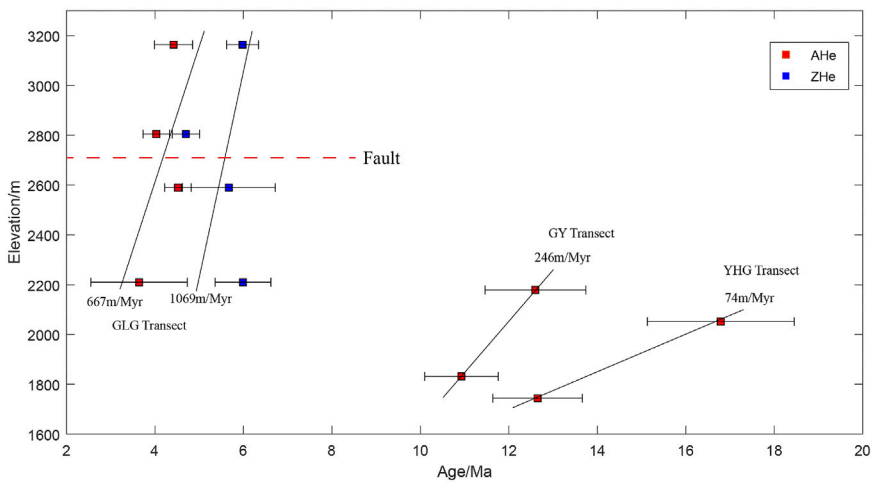

FIGURE 4 | Age–elevation relationship diagram of low-temperature thermochronological data of Ahe and Zhe.

the relationship between age and altitude (Glotzbach et al., 2011). Results show that the exhumation rate of the YHG transect that is located in the footwall of the Gaoligong shear zone is the lowest, with approximately 74 m/Ma at 18–12 Ma. At 6–2 Ma, the exhumation rate at GLG transect is 667–1,069 m/Ma, which is 9–14 times that of the former. This finding reveals the significant difference between the Ailaoshan mountain and the Gaoligong Mountain. The GY transect is located in the west of the Tengchong Basin, which may be affected by the Nabang fault, resulting in a high exhumation rate.

Fission Track Analysis

Apatite fission track (AFT) analyses of samples of GLG transect were conducted at the Neotectonic Geochronology Laboratory at the Institute of Geology, China Earthquake Administration. Apatite fission track ages were obtained using the LA-ICPMS

TABLE 4 | Results of the fission track analysis of apatite in the Gaoligong ductile shear zone(GLGSZ).

Sample ID (TC)	Latitude	Longitude	Elevation (m)	ρs	Ns ($\times10^5 cm^{-2}$)	Nc	P(X^2) (%)	Age (Ma)	±σ (Ma)	Dpar (μm±SD)
2008	25.284	98.703	2210	0.269	85	35	100	7.46	0.81	1.54 ± 0.25
2009	25.286	98.716	2590	0.852	87	29	58	8.19	0.94	1.82 ± 0.3
2010	25.29	98.728	2805	0.897	229	30	59	3.26	0.22	1.7 ± 0.25
2011	25.291	98.737	3164	1.186	208	30	74	4.25	0.3	1.6 ± 0.15

Rho-S, spontaneous track density; Ni, total number of induced tracks; Rho-I, induced track density; Nd, number of tracks counted on dosimeter; Rho-D, effective fission-track densities for the fluence monitor; P (χ^2) (%), probability of obtaining Chi-square value (χ^2); Age, ±1σ; ζ value is 370.1 ± 11.2; all samples pass the Chi-squared test, and therefore, reported ages are all pooled ages; Dpar, average etch pit diameter of fission tracks.

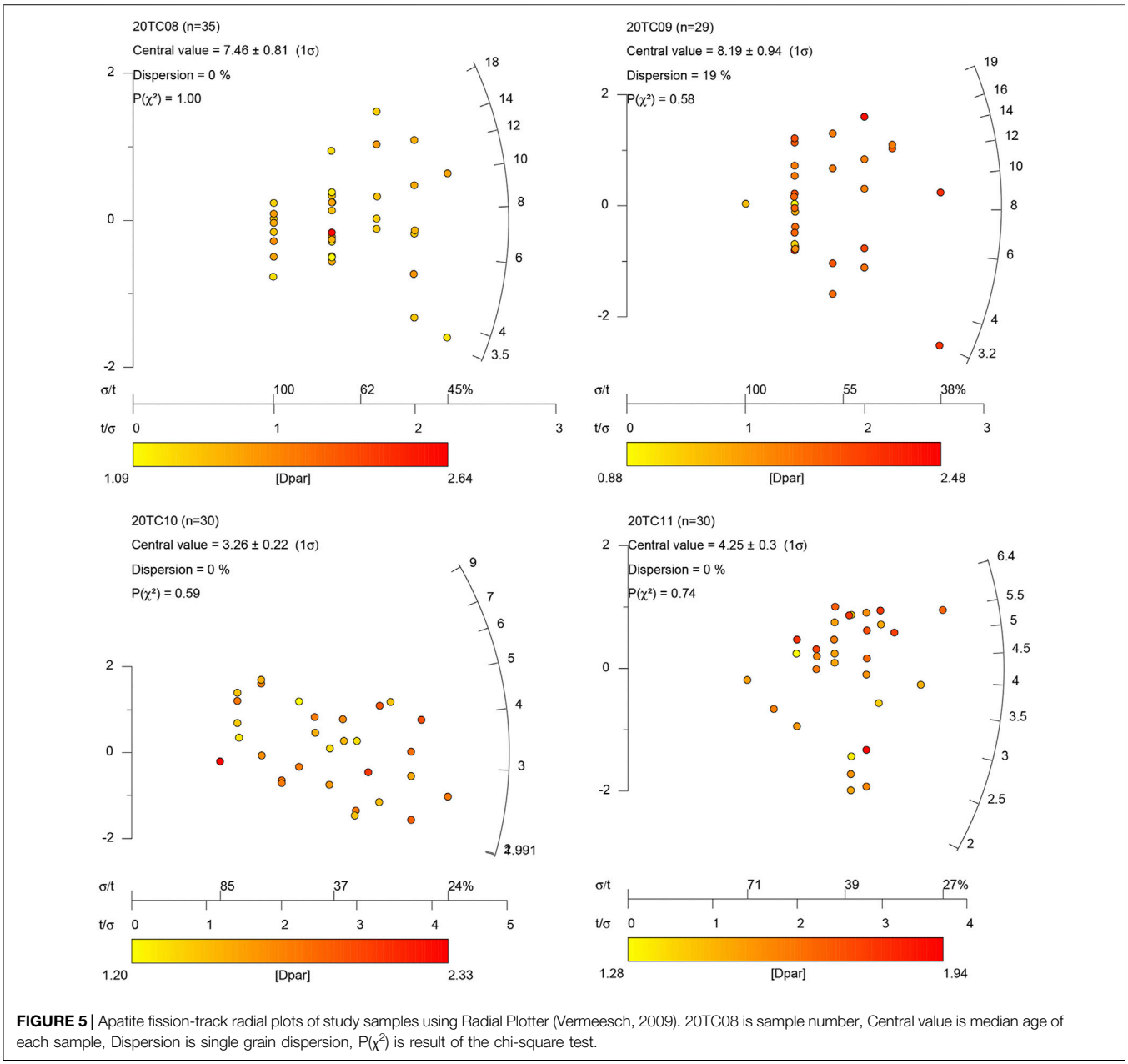

FIGURE 5 | Apatite fission-track radial plots of study samples using Radial Plotter (Vermeesch, 2009). 20TC08 is sample number, Central value is median age of each sample, Dispersion is single grain dispersion, P(χ^2) is result of the chi-square test.

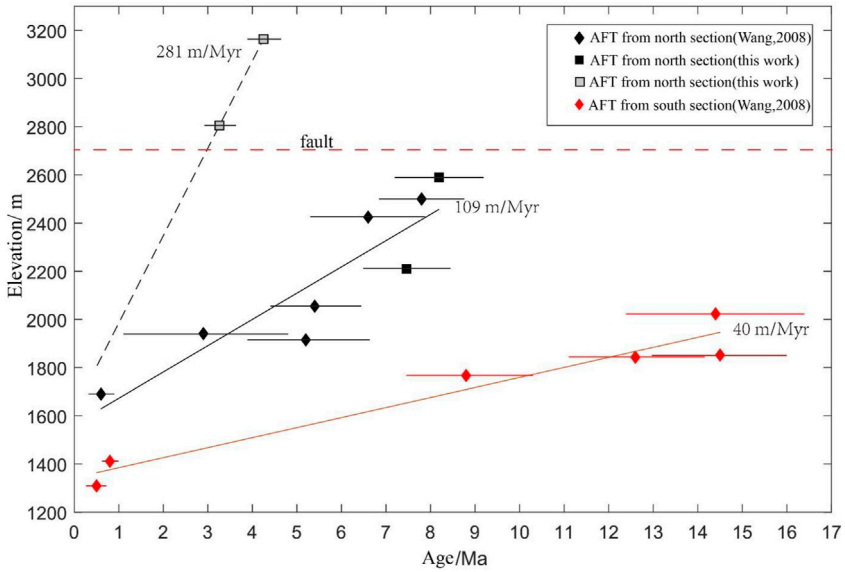

FIGURE 6 | Age–elevation relationship diagram of AFT data in different transects of the Gaoligong shear zone.

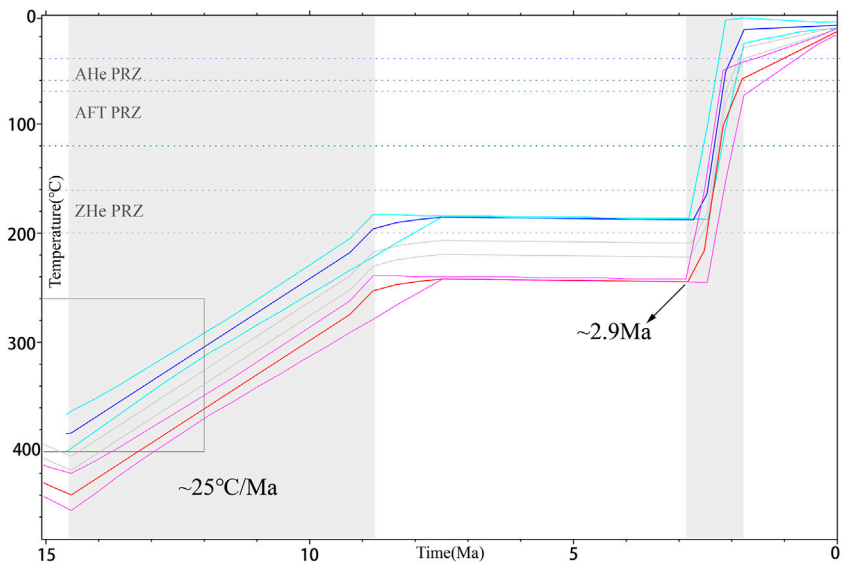

FIGURE 7 | Thermal modelling of the GLG transect using QTQt (Gallagher, 2012). The grey box indicates the initial constraint. For the uppermost thermal history, the thin blue lines depict 95% confidence intervals, reflecting the uncertainty in the inferred thermal history alone. For the lowermost thermal history, the thin red lines show 95% confidence intervals, reflecting combined uncertainties in the inferred thermal history and temperature offset. The provided AHe ages are uncorrected for the comparison of observed and predicted data.

method (Hasebe et al., 2004; Lisker et al., 2009; Hasebe et al., 2013) and calculated by the zeta calibration method (Pang et al., 2017). Age-calibration standard is Durango apatite (31.4 ± 0.5 Ma). The National Bureau of Standards trace element glass NIST612 were used as an external standard to measure the signal intensity the test. Uranium measurement was carried out under the LA-ICPMS equipment. Spontaneous fission tracks in apatite were etched in 5.5N HNO3 at 21°C for 20 s. Fission tracks and track-length measurements were counted on a Zeiss Axioplan2 microscope, using a dry objective with magnification of 1000. All analyses were performed by J. Z Pang whose lab had a weighted mean zeta of Apatite-Zeta NIST612=1940 ± 50 while using the above methods and standards. Apatite fission track data are listed in supplement **Table 4**.

In the GLG transect, The AFT ages were from 3.2 to 8.1 Ma (**Figure 5** and **Table 4**). All ages have passed the P(χ^2) test, and the

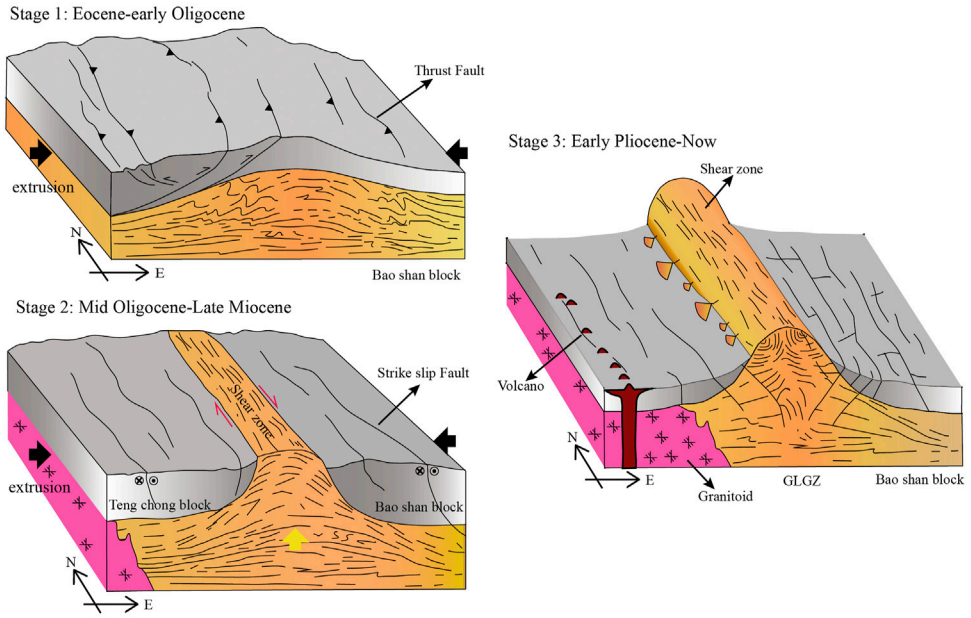

FIGURE 8 | A simplified conceptual model illustrating the tectonic evolution and uplift and exhumation process of the Gaoligong shear zone (GLGSZ). During the Eocene–Early Oligocene, the crust might have been shortened and thickened in the southeastern margin of the Qinghai–Tibet Plateau, resulting in the weakening of the rheology of the middle and lower crust. Right-lateral ductile shear occurred from the Middle Oligocene to Late Miocene. During this time, the GLGSZ acted as a channel for vertical extrusion of low-viscosity crustal materials in the deep. Since the early Pleistocene, the Gaoligong Mountain has been further uplifted and exposed, the middle and upper crust has been dominated by brittle deformation, the plates have been staggered by active faults, and magmatic activity has been enhanced.

discrete value is low, indicating a single age group. Owing to the small number of tracks in all samples, only one sample, 20TC10, had a track length, and its average track length was 12.18–16.02 μm. The Dpar values of all samples were between 1.3 and 2.1 μm. Together with the AFT data of Wang et al. (2018) (**Figure 4A**), we found that the exhumation rate of the south section of GLGSZ is ~40 m/Ma and the exhumation rate of the north section is ~109 m/Ma. We collected some samples at the top of the north section (altitude >2,800 m), and the exhumation rate is approximately 281 m/Ma. Therefore, since the Miocene, the exhumation rate in the north section of GLGSZ has become significantly faster than that in the south section, and the exhumation rate at the top of the north section is faster than that at the bottom (**Figure 6**). The two samples at the top of the vertical transect are abnormally young, and it may be related to the activity of the fault at elevations of about 2,700 m (**Figure 6**).

Modeling

In order to study the history of thermal evolution of the GLG, we used the QTQt program, which uses the Markov chain Monte Carlo method. To simulate the thermal history (Gallagher et al., 2005; Gallagher, 2012) of the GLG, we inverted the thermochronological ages of different elevations. In this study, AHe, ZHe, and AFT data of the GLG profile were also modelled using the QTQt program. According to the published $^{40}Ar/^{39}Ar$ ages of granite and mylonite-biotite, we set the initial temperature of the GLG transect at 330 ± 70°C and the corresponding age at 17 ± 5 Ma (Akciz, 2004; Lin et al., 2009; Zhang et al., 2010; Zhang et al., 2012). The simulation was carried out for 400,000 iterations, of which 200,000 each were used for burn-in inversion and joint simulation of three types of data. Using a higher number of iterations did not significantly improve the simulation results.

The inversion simulation of the GLG profile revealed two stages of rapid cooling (**Figure 7**). The first stage occurred between 14.5 and 8.8 Ma, and some samples even reached the partial retention zone (PRZ) of zircon, and then experienced a slow cooling process lasting approximately 6 Ma. Subsequently, the cooling rate began to increase at ~2.9 Ma, and all the samples were denuded to the near surface. The rate of the second cooling was much higher than that of the first. According to the thermal history model, the two cooling temperatures are similar. The estimation of the exhumation quantity depends on the low-temperature gradient, but this parameter is often unknown. Here, we assume that the range of the low-temperature gradient is 30–40°C/km, which is similar to related research conducted in nearby areas (Clark et al., 2005; Wang et al., 2018), and conclude that the shear zone may have experienced 5–6 km of exhumation at this stage. In summary, the inversion results of the GLG profile show that the GLGSZ experienced two rapid exhumation stages in the Miocene and Pliocene.

DISCUSSION

History of Exhumation of the Gaoligong Shear Zone

The GLGSZ divides the Baoshan and Tengchong Blocks and is mainly composed of high-grade metamorphic rocks and intrusive

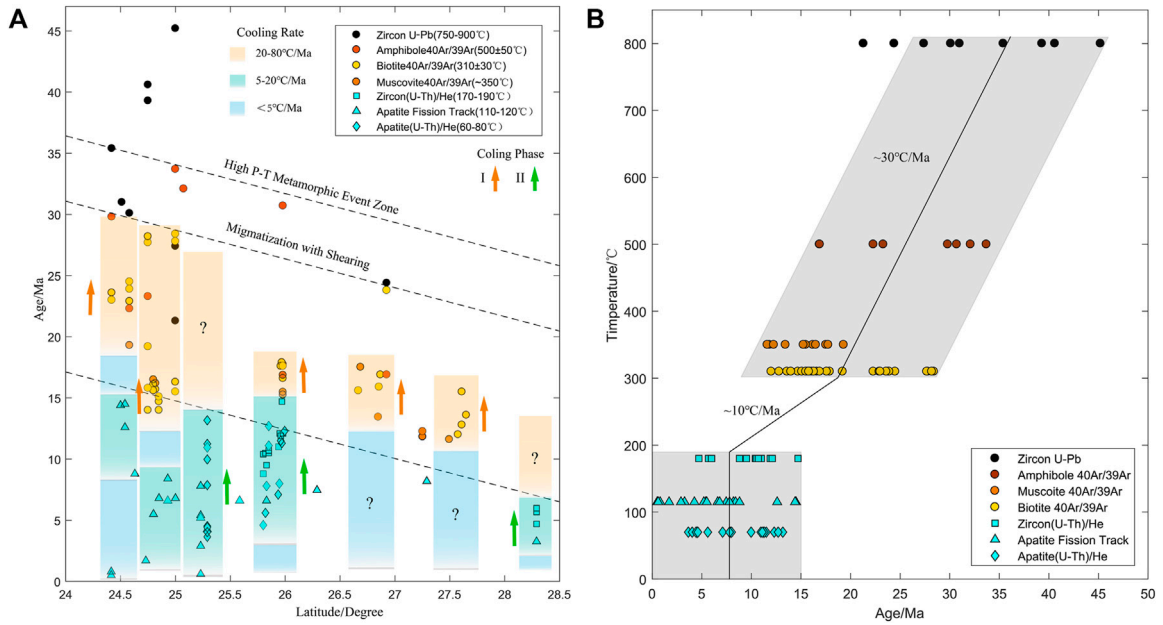

FIGURE 9 | Summary of thermochronological data for the Gaoligong shear zone (GLGSZ). Ages are compiled from Wang et al. (2008, 2018), Akciz et al. (2008), Gilley et al. (2003), Lin et al. (2009), Zhang et al. (2012, 2017), Xu et al. (2015), Ji et al. (2000), Ding (1991), Tang et al. (2016, 2020), and this study. A synthesis of these data suggests differential thermal histories along the latitude. **(A)** The GLGSZ experienced prominent and rapid cooling from a high temperature of >500–190°C at a rate of 20–80°C/Ma during 30–15 Ma at 25° north latitude. A lower-magnitude accelerated cooling event took place during 15–0 Ma at 24.5°–26° north latitude. **(B)** Age-temperature relationship of different thermochronological data of the GLGSZ.

granite. The foliation and mineral lineation parallel to the mountain's strike show significant stretching and the movement direction of the dextral shear (Socquet and Pubellier, 2005; Qi et al., 2012). The U/Pb age of high-temperature metamorphic zircon in the Gaoligong right strike-slip shear zone is 52–46 Ma (Xu et al., 2015), which indicates that the initial time of the India–Asia oblique collision outside the East Indian tectonic segment may be around 50 Ma. ^{40}Ar-^{39}Ar dating shows that the right strike slip of the Gaoligong shear zone started at 32 Ma, and its main activities were in three stages during 27–29 Ma, 18–17 Ma, and 14 Ma (Wang et al., 2008). The mylonite of the Gaoligong Group thrusted on to the Eocene strata (Qi et al., 2012), which also indicated that the GLGSZ was uplifted after the Eocene. The data of zircon U-Pb and mica K-Ar show that the GLGSZ has rapidly cooled 18 Ma ago (Lin et al., 2009). Ji et al. (2000) measured the main active ages of the Gaoligong strike-slip fault zone, and their active ages were estimated at 24–19 Ma and 14–11 Ma, respectively. In the Middle Miocene (~18 Ma), the GLGSZ was connected with the Jiali fault zone and began to cooperate with a dextral strike-slip movement (Lin et al., 2009). The dextral shear process of the GLGSZ caused partial melting of the crust, resulting in the intrusion of many light-coloured granites with U-Pb ages of ~24–21 Ma (Song et al., 2010). The ^{40}Ar/^{39}Ar dating of muscovite and biotite recorded rapid exhumation of the GLGSZ at 18–11 Ma (Akciz, 2004; Wang et al., 2006; Lin et al., 2009; Zhang et al., 2012). Mylonitization of rocks occurred at 20–12 Ma (Zhong et al., 1991; Wang et al., 1998), which is the same period as when rapid exhumation and dextral ductile shear of the GLGSZ occurred. Therefore, in the early Eocene, the outer side of the East Indian tectonic node began to collide with the Lhasa plate, and dynamic metamorphism formed high-grade metamorphic rocks with significant directional minerals and intrusion of magma. The GLGSZ actively responded to the continuous compression of the northeast corner of the Indian plate and moved synchronously with the Eastern Himalayan syntaxis (EHS). The early–middle Miocene EHS activity dominated the evolution of large strike-slip fault zones in this area. The GLGSZ experienced dextral shear, rapid exhumation, mylonitization, and magmatic intrusion of the mountain at the same time. In the early Miocene, the time of activity of the GLGSZ coincided with that of the Honghe River–Ailao Mountain ductile shear zone in the east, and it was connected with the Jiali fault and began to cooperate with the dextral strike-slip movement. In the middle Miocene, the expansion of the Andaman Sea and the dextral strike-slip movement of the Shijie fault were consistent. From the Jiali fault to Gaoligong ductile shear zone and then to the Sagaing fault, a huge western boundary of the Indosinian block was formed. After experiencing the complex tectonic movement in the Miocene, the basic geomorphic pattern of the southeastern margin of the Qinghai–Tibet Plateau was laid.

Possible Contribution of the Quaternary Glaciation to the Rapid Exhumation of the GLGSZ

Low-temperature thermal chronological data of AHe, ZHe, and AFT showed that the GLGSZ stopped rapid cooling at ~10 Ma, which is also in good agreement with our modeling results.

However, ZHe data of the Chongshan Mountain ductile shear zone shows that its rapid cooling also stopped at ~10 Ma (Wang et al., 2018), which indicates that the large-scale ductile shear zone in the southeastern margin of the Qinghai–Tibet Plateau almost moved in concert in the Miocene. The rapid uplift of the surface in western Sichuan occurred during 8–1 Ma (Kirby et al., 2002; Clark et al., 2005), but it may be later than 5 Ma in the Three Rivers Region (Schoenbohm et al., 2006). The simulation of thermal history using comprehensive data shows that the latest rapid cooling event of the GLGSZ began at 2.9 Ma, which was difficult to discern in past research because of the influence of the precision of testing instruments and equipment and the quality of samples. This cooling event lasted for ~1 Ma, and the cooling rate was faster than that in the Miocene. Assuming that the low temperature gradient was 30–40°C/Km, the stratum exhumation thickness of this event reached 5–6 km at 2.9 Ma. This period is very close to the period of the global Quaternary glaciation. Glacial landforms such as U-shaped valleys are widely distributed in the study area, which is one of the most extensive glacier areas in the southeastern margin of the Qinghai–Tibet Plateau (Fu et al., 2013). The study area is located in the upper reaches of the Three River Basin, and this rapid cooling event is related to the rapid downcutting by the river (Yang et al., 2015). This period was also a period of intense activity of volcanoes and active faults, which may also have accelerated the cooling process of the GLGSZ. Yang et al. (2015) tested seven blocks of AHe samples near EHS and believed that the erosion in this area significantly accelerated at ~2 Ma. Therefore, as the global climate in the early Pleistocene entered the ice age, the ice erosion in the study area intensified, and the glacier landform developed widely. Affected by the uplift of mountains and climate, water vapor from the Pacific Ocean and the Indian Ocean was blocked to form rainfall, which accelerated the erosion of landforms and the undercutting of rivers. In addition, brittle faults and volcanic activities were also significantly intensified. The Baoshan Block located in the east of the GLGSZ is fragmented by fault depression. The Tengchong Block located in the west of the GLGSZ is mainly composed of granite and basalt. Hundreds of volcanic cones are scattered inside the basin, and volcanic activities are mainly concentrated in the Pleistocene (Li et al., 2019). At an altitude of 2,200 m, the average exhumation rate of the GLGSZ is 3–4 times that of the Tengchong Block. Then, under the combined action of climate, river erosion, fault activity, and overall uplift of the crust, the study area underwent rapid cooling in the early Pleistocene (**Figure 8**).

Dynamic Model of Growth and Propagation of the Plateau

In terms of the genesis of the unique geomorphological features in the southeastern margin of the Qinghai–Tibet Plateau and its geodynamic model, our results comparatively support the lower crustal flow model. The key geological and geomorphological supporting evidence in this model is that there is a "plane-like structure" in the southeast edge of the plateau that stretches for thousands of kilometres in the region before uplift, from the boundary line of the internal/external water system in the plateau to the low altitude of the South China Sea. This remains in the deep valley highland (Clark et al., 2006). Recent geophysical research results explain that there are two uniform low-velocity zones in the middle and lower crust at the EHS (Yao et al., 2010; Sun et al., 2014; Bao et al., 2015). The low-speed zone on the west side is located below the GLGSZ and CSSZ (Bao et al., 2015). Although these results cannot accurately define the uplift process of the plateau during the Quaternary period, inferences can be drawn based on other factors. The uplift process is caused by different exhumation rates in the north and south of the GLGSZ, gravity creep flow rising from the middle of the plateau to its edge, occurrence of tilting uplift in the southeast direction, and upward pushing force generated by the continuous thickening of the middle and lower crust providing the main source of material and power in the southeast edge, and spontaneous river attack and accelerated exhumation since Pliocene leading to unloading and acceleration of erosion to break the balance of the crust. In addition, Wang et al. (2018) suggested that the GLGSZ is high in the north and low in the south, which is the result of gravity collapse, but the present study does not support this conclusion. According to data presented in **Figure 9**, the exhumation rate in the north of the GLGSZ is higher than that in the south, and hence, the closer to the north, the higher the corresponding altitude. Yang et al. (2015) estimated the erosion rate in this area through the longitudinal profile of the river. Similarly, the erosion rate in the north is higher than that in the south, and no re-heating process was evident based on our thermal chronological data. If the rapid exhumation of the GLGSZ in the Pliocene is related to the influx of lower crust materials, then our low-temperature thermochronology data recorded the events of this process accurately. This can also explain the special topography of the GLGSZ, which is high in the north and low in the south, and the spatiotemporal variations show that the uplift gradually reduces from north to south.

CONCLUSION

In this study, the history of thermal evolution of the ductile strike-slip shear zone in the Gaoligong Mountain in the southeast margin of the Qinghai–Tibet Plateau was analysed using AHe, ZHe, and AFT to reveal the rapid cooling process in two stages of the early Miocene–middle Miocene (~14.5 Ma) and early Pleistocene (~2.9 Ma). In the Eocene, the northeast corner of the Indian plate collided obliquely with the Eurasian plate in the eastern structure, and the lithosphere of the eastern syntaxis in the region thickened and started the dextral strike-slip movement synchronously. During the early Miocene–middle Miocene period, influenced by the plateau uplift and structural adjustment of the EHS, the GLGSZ continued the dextral shear movement, and was rapidly exposed. In the early Pleistocene, under the combined action of rapid incised erosion of rivers and continuous activity of brittle faults, the GLGSZ was rapidly denuded again, and at this time, the exhumation rate significantly increased, and the rocks were denuded to the surface. The

exhumation and erosion rates of the GLGSZ were different at different latitudes, and this tilting type of the uplift has formed a special landform that is high in the north and low in the south.

DATA AVAILABILITY STATEMENT

The original contributions presented in the study are included in the article/Supplementary Material, further inquiries can be directed to the corresponding author.

AUTHOR CONTRIBUTIONS

JW gathered and prepared all data, performed all calculations, and created all figures. He developed the model and modelling procedure with the guidance of HZ. FS and NL contributed to the discussion of results and participated in the writing of the paper. YW, LN, and JP prepared the samples and conducted the experiments. JW and YZ conducted the field work.

FUNDING

This work was supported by the Institute of Geology, China Earthquake Administration (IGCEA 2003) and Jilin Changbaishan Volcano National Observation and Research Station, IGCEA (NORSCBS21-06).

ACKNOWLEDGMENTS

I would like to thank China Scholarship Council for sponsoring me during my studies at the University of Glasgow.

REFERENCES

Akciz, O. S. (2004). *Structure and Geochronological Constraints on the Ductile Deformation Observed along the Gaoligong Shan and Chong Shan Shear Zones*. Yunnan (China)[Boston(MA)]: Massachusetts Institute of Technology. [dissertation thesis].

Akciz, S., BurchfielCrowley, B. C. J. L., Crowley, J. L., Jiyun, Y., and Liangzhong, C. (2008). Geometry, Kinematics, and Regional Significance of the Chong Shan Shear Zone, Eastern Himalayan Syntaxis, Yunnan, China. *Geosphere* 4, 292–314. doi:10.1130/GES00111.1

Allen, C. R., Gillespie, A. R., Yuan, H., Sieh, K. E., Buchun, Z., and Chengnan, Z. (1984). Red River and Associated Faults, Yunnan Province, China: Quaternary Geology, Slip Rates, and Seismic hazard. *Geol. Soc. America Bull.* 95, 6862–7700. doi:10.1130/0016-7606(1984)952.0.CO10.1130/0016-7606(1984)95<686:rraafy>2.0.co;2

Ault, A. K., and Flowers, R. M. (2012). Is Apatite U-Th Zonation Information Necessary for Accurate Interpretation of Apatite (U-Th)/He Thermochronometry Data? *Geochimica et Cosmochimica Acta* 79, 60–78. doi:10.1016/j.gca.2011.11.037

Bao, X., Sun, X., Xu, M., Eaton, D. W., Song, X., Wang, L., et al. (2015). Two Crustal Low-Velocity Channels beneath SE Tibet Revealed by Joint Inversion of Rayleigh Wave Dispersion and Receiver Functions. *Earth Planet. Sci. Lett.* 415, 16–24. doi:10.1016/j.epsl.2015.01.020

Chang, Z., Chen, G., and Yu, J. (2011). Geological Evidence of Activity along the Dayingjaing Fault since Late Pleistocene. *Seismology Geology*. 33, 877–888. (in Chinese with English abstract).doi:10.3969/j.issn.0253-4967.2011.04.012

Clark, M. K., House, M. A., Royden, L. H., Whipple, K. X., Burchfiel, B. C., Zhang, X., et al. (2005). Late Cenozoic Uplift of southeastern Tibet. *Geol* 33, 525–528. doi:10.1111/1755-6724.12148_210.1130/g21265.1

Clark, M. K., Royden, L. H., Whipple, K. X., Burchfiel, B. C., Zhang, X., and Tang, W. (2006). Use of a Regional, Relict Landscape to Measure Vertical Deformation of the Eastern Tibetan Plateau. *J. Geophys. Res.* 111, a–n. doi:10.1029/2005jf000294

Dewey, J. F., Cande, S. C., and Pitman, W. C. I. (1989). Tectonic Evolution of the India/Eurasia Collision Zone. *Eclogae Geologicae Helv.* 82, 717–734. doi:10.111/j.1365-3091.1989.tb00830.x

Ding, L. (1991). *The Characteristics of Deformation and Tectonic Implications in South Gaoligong, Western Yunnan, China*. [master thesis]. Beijing]:: Institure of Geology, Chinese Academy of Science. doi:10.1111/j.1365-3091.1989.tb00830.x

Dong, Y., Cao, S., Neubauer, F., Wang, H., Li, W., and Genser, J. (2021). Exhumation of the Crustal-Scale Gaoligong Strike-Slip Shear belt in SE Asia. *J. Geol. Soc*. doi:10.6084/m9.figshare.c.5598365.v110.1144/jgs2021-038

England, P., and Molnar, P. (1990). Surface Uplift, Uplift of Rocks, and Exhumation of Rocks. *Geol* 18, 1173–1177. doi:10.1130/0091-7613(1990)018<1173:suuora>2.3.co;2

Farley, K. A. (2000). Helium Diffusion from Apatite: General Behavior as Illustrated by Durango Fluorapatite. *J. Geophys. Res.* 105, 2903–2914. doi:10.1029/1999jb900348

Farley, K. A. (2002). (U-Th)/He Dating: Techniques, Calibrations, and Applications. *Rev. Mineralogy Geochem.* 47, 819–844. doi:10.2138/rmg.2002.47.18

Flowers, R. M., Ketcham, R. A., Shuster, D. L., and Farley, K. A. (2009). Apatite (U-Th)/He Thermochronometry Using a Radiation Damage Accumulation and Annealing Model. *Geochimica et Cosmochimica Acta* 73, 2347–2365. doi:10.1016/j.gca.2009.01.015

Fu, P., Harbor, J. M., Stroeven, A. P., Hättestrand, C., Heyman, J., and Zhou, L. (2013). Glacial Geomorphology and Paleoglaciation Patterns in Shaluli Shan, the southeastern Tibetan Plateau - Evidence for Polythermal Ice Cap Glaciation. *Geomorphology* 182, 66–78. doi:10.1016/j.geomorph.2012.10.030

Gallagher, K., Stephenson, J., Brown, R., Holmes, C., and Fitzgerald, P. (2005). Low Temperature Thermochronology and Modeling Strategies for Multiple Samples 1: Vertical Profiles. *Earth Planet. Sci. Lett.* 237, 193–208. doi:10.1016/j.epsl.2005.06.025

Gallagher, K. (2012). Transdimensional Inverse thermal History Modeling for Quantitative Thermochronology. *J. Geophys. Res.* 117, a–n. doi:10.1029/2011JB008825

Gilley, L. D., Harrison, T. M., Leloup, P. H., Ryerson, F. J., Lovera, O. M., and Wang, J.-H. (2003). Direct Dating of Left-Lateral Deformation along the Red River Shear Zone, China and Vietnam. *J. Geophys. Res.* 108, 14–21. doi:10.1029/2001JB001726

Glotzbach, C., van der Beek, P. A., and Spiegel, C. (2011). Episodic Exhumation and Relief Growth in the Mont Blanc Massif, Western Alps from Numerical Modelling of Thermochronology Data. *Earth Planet. Sci. Lett.* 304, 417–430. doi:10.1016/j.epsl.2011.02.020

Guenthner, W. R., Reiners, P. W., Ketcham, R. A., Nasdala, L., and Giester, G. (2013). Helium Diffusion in Natural Zircon: Radiation Damage, Anisotropy, and the Interpretation of Zircon (U-Th)/He Thermochronology. *Am. J. Sci.* 313, 145–198. doi:10.2475/03.2013.01

Hasebe, N., Barbarand, J., Jarvis, K., Carter, A., and Hurford, A. J. (2004). Apatite Fission-Track Chronometry Using Laser Ablation ICP-MS. *Chem. Geology.* 207, 135–145. doi:10.1016/j.chemgeo.2004.01.007

Hasebe, N., Tamura, A., and Arai, S. (2013). Zeta Equivalent Fission-Track Dating Using LA-ICP-MS and Examples with Simultaneous U-Pb Dating. *Isl. Arc* 22, 280–291. doi:10.1111/iar.12040

Houseman, G., and England, P. (1993). Crustal Thickening versus Lateral Expulsion in the Indian-Asian continental Collision. *J. Geophys. Res.* 98 (12), 12233–12249. doi:10.1029/93JB00443

Ji, J. Q., Zhong, D. L., Sang, H. Q., Qiu, J., and Hu, S. L. (2000). Dating of Two Metamorphic Events on the basalt Granulite from the Nabang Area on the Border of China and Burma. *Acta Petrologica Sinica* 16, 227–232. doi:10.2118/64226-PA

Kirby, E., Reiners, P. W., Krol, M. A., Whipple, K. X., Hodges, K. V., Farley, K. A., et al. (2002). Late Cenozoic Evolution of the Eastern Margin of the Tibetan Plateau: Inferences from40Ar/39Ar and (U-Th)/He Thermochronology. *Tectonics* 21, 1. doi:10.1029/2000TC001246

Kristen Clark, M., and Handy Royden, L. (2000). Topographic Ooze: Building the Eastern Margin of Tibet by Lower Crustal Flow. *Geology* 28, 703–706. doi:10.1130/0091-7613(2000)028<0703:tobtem>2.3.co;2

Li, H.-A., Dai, J.-G., Xu, S.-Y., Liu, B.-R., Han, X., Wang, Y.-N., et al. (2019). The Formation and Expansion of the Eastern Proto-Tibetan Plateau: Insights from Low-Temperature Thermochronology. *J. Asian Earth Sci.* 183, 103975. doi:10.1016/j.jseaes.2019.103975

Li, N., Zhao, Y.-W., Zhang, L.-Y., and Wang, J.-L. (2020). The Quaternary Eruptive Sequence of the Tengchong Volcanic Group, Southwestern China. *Lithos* 354-355, 105173. doi:10.1016/j.lithos.2019.105173

Lin, T.-H., Lo, C.-H., Chung, S.-L., Hsu, F.-J. Yeh., Yeh, M.-W., Lee, T.-Y., et al. (2009). 40Ar/39Ar Dating of the Jiali and Gaoligong Shear Zones: Implications for Crustal Deformation Around the Eastern Himalayan Syntaxis. *J. Asian Earth Sci.* 34, 674–685. doi:10.1016/j.jseaes.2008.10.009

Lisker, F., Ventura, B., and Glasmacher, U. A. (2009). Apatite Thermochronology in Modern Geology. *Geol. Soc. Lond. Spec. Publications* 324, 1–23. doi:10.1144/SP324.1

Liu, J., Zeng, L., Ding, L., Tapponnier, P., Gaudemer, Y., Wen, L., et al. (2009). Tectonic Geomorphology|active Tectonics and Lower Crustal Channel Flow Hypothesis of the southeastern Tibetan Plateau. *Chin. J. Geology.* 44, 1227–1255. doi:10.3321/j.issn:0563-5020.2009.04.014

Liu-Zeng, J., Tapponnier, P., Gaudemer, Y., and Ding, L. (2008). Quantifying Landscape Differences across the Tibetan Plateau: Implications for Topographic Relief Evolution. *J. Geophys. Res.* 113, F04018. doi:10.1029/2007JF000897

Liu-Zeng, J., Zhang, J., McPhillips, D., Reiners, P., Wang, W., Pik, R., et al. (2018). Multiple Episodes of Fast Exhumation since Cretaceous in Southeast Tibet, Revealed by Low-Temperature Thermochronology. *Earth Planet. Sci. Lett.* 490, 62–76. doi:10.1016/j.epsl.2018.03.011

Mitchell, A. H. G. (1993). Cretaceous-Cenozoic Tectonic Events in the Western Myanmar (Burma)-Assam Region. *J. Geol. Soc.* 150, 1089–1102. doi:10.1144/gsjgs.150.6.1089

Molnar, P., and England, P. (1990). Late Cenozoic Uplift of Mountain Ranges and Global Climate Change: Chicken or Egg? *Nature* 346, 29–34. doi:10.1038/346029a0

Molnar, P., and Tapponnier, P. (1978). Active Tectonics of Tibet. *J. Geophys. Res.* 83, 5361–5376. doi:10.1029/JB083IB11p05361

Naiman, Y., Sobel, E. R., Millar, I., Stockli, D. F., Govin, G., Lisker, F., et al. (2020). The Exhumation of the Indo-Burman Ranges, Myanmar. *Earth Planet. Sci. Lett.* 530, 115948. doi:10.1016/j.epsl.2019.115948

Ouimet, W., Whipple, K., Royden, L., Reiners, P., Hodges, K., and Pringle, M. (2010). Regional Incision of the Eastern Margin of the Tibetan Plateau. *Lithosphere* 2, 50–63. doi:10.1130/l57.1

Qi, X., Zhao, Y., Zhu, L., and Li, Z. (2012). Discovery of High-Pressure Pelitic Granulite in Ailaoshan Orogenic belt, southeastern Tibet and its Tectonic Implications. *Acta Petrologica Sinica* 28, 1846.

Reiners, P. W., and Farley, K. A. (2001). Influence of crystal Size on Apatite (U-Th)/He Thermochronology: An Example from the Bighorn Mountains, Wyoming. *Earth Planet. Sci. Lett.* 188, 413–420. doi:10.1016/S0012-821X(01)00341-7

Reiners, P. W. (2005). Zircon (U-Th)/He Thermochronometry. *Rev. Mineralogy Geochem.* 58, 151–179. doi:10.2138/rmg.2005.58.6

Royden, L. H., Burchfiel, B. C., King, R. W., Wang, E., Chen, Z., Shen, F., et al. (1997). Surface Deformation and Lower Crustal Flow in Eastern Tibet. *Science* 276, 788–790. doi:10.1126/science.276.5313.788

Royden, L. H., Burchfiel, B. C., and van der Hilst, R. D. (2008). The Geological Evolution of the Tibetan Plateau. *Science* 321, 1054–1058. doi:10.1126/science.1155371

Shen, X., Tian, Y., Wang, Y., Wu, L., Jia, Y., Tang, X., et al. (2021). Enhanced Quaternary Exhumation in the Central Three Rivers Region, Southeastern Tibet. *Front. Earth Sci.* 9, 741491. doi:10.3389/feart.2021.741491

Socquet, A., and Pubellier, M. (2005). Cenozoic Deformation in Western Yunnan (China-Myanmar Border). *J. Asian Earth Sci.* 24, 495–515. doi:10.1016/j.jseaes.2004.03.006

Song, S., Niu, Y., Wei, C., Ji, J., and Su, L. (2010). Metamorphism, Anatexis, Zircon Ages and Tectonic Evolution of the Gongshan Block in the Northern Indochina Continent-An Eastern Extension of the Lhasa Block. *Lithos* 120, 327–346. doi:10.1016/j.lithos.2010.08.021

Sun, X., Bao, X., Xu, M., Eaton, D. W., Song, X., Wang, L., et al. (2014). Crustal Structure beneath SE Tibet from Joint Analysis of Receiver Functions and Rayleigh Wave Dispersion. *Geophys. Res. Lett.* 41, 1479–1484. doi:10.1002/2014GL059269

Tang, Y., Wang, D. B., Liao, S. Y., Wang, B. D., Yin, F. G., and Wang, L. Q. (2016). Geochronological Characterization and Regional Tectonic Implication of the Leucogranites in the Southern Segment of Gaoligong Metamorphic Zone, Western Yunnan. *Acta Petrologica Sinica* 32, 2347–2366. doi:10.1007/s10114-016-4736-8

Tang, Y., Wang, D., Liao, S., Wang, B., and Yin, F. (2020). Fabrics and 40Ar/39Ar Ages of Metamorphic Rocks in the Gaoligong Tectonic belt: Implications for Cenozoic Metamorphism and Deformation in the SE Tibetan Plateau. *J. Asian Earth Sci.* 192, 104270. doi:10.1016/j.jseaes.2020.104270

Tapponnier, P., Peltzer, G., Le Dain, A. Y., Armijo, R., and Cobbold, P. (1982). Propagating Extrusion Tectonics in Asia: New Insights from Simple Experiments with Plasticine. *Geol* 10, 611–616. doi:10.1130/0091-7613(1982)10<611:petian>2.0.co;2

Tapponnier, P., Zhiqin, X., Roger, F., Meyer, B., Arnaud, N., Wittlinger, G., et al. (2001). Oblique Stepwise Rise and Growth of the Tibet Plateau. *Science* 294, 1671–1677. doi:10.1126/science.105978

Wang, C., Liang, C., Deng, K., Huang, Y., and Zhou, L. (2018). Spatiotemporal Distribution of Microearthquakes and Implications Around the Seismic Gap between the Wenchuan and Lushan Earthquakes. *Tectonics* 37, 2695–2709. doi:10.1029/2018TC005000

Wang, C., Zhao, X., Liu, Z., Lippert, P. C., Graham, S. A., Coe, R. S., et al. (2008). Constraints on the Early Uplift History of the Tibetan Plateau. *Proc. Natl. Acad. Sci. U.S.A.* 105 (13), 4987–4992. doi:10.1073/pnas.0703595105

Wang, E., Burchfiel, B. C., Royden, L. H., Chen, L. Z., Chen, J. S., Li, W. X., et al. (1998). *Late Cenozoic Xianshuihe-Xiaojiang, Red River, and Dali Fault Systems of Southwestern Sichuan and Central Yunnan*. ChinaBoulder: Geological Society of America Publications.

Wang, E., KirbyFurlong, E. K. P., Furlong, K. P., van Soest, M., Xu, G., Shi, X., et al. (2012). Two-phase Growth of High Topography in Eastern Tibet during the Cenozoic. *Nat. Geosci* 5, 640–645. doi:10.1038/ngeo1538

Wang, G., Wan, J., Wang, E., Zheng, D., and Li, F. (2008). Late Cenozoic to Recent Transtensional Deformation across the Southern Part of the Gaoligong Shear Zone between the Indian Plate and SE Margin of the Tibetan Plateau and its Tectonic Origin. *Tectonophysics* 460, 1–20. doi:10.1016/j.tecto.2008.04.007

Wang, G., Wan, J., and Zhao, W, E. (2006). Late Cenozoic Tectonics-Gravity Collapse and its Causes in the Southern Gaoligong Mountains. *Acta Geologica Sinica* 9, 1262–1273. (in Chinese). doi:10.3321/j.issn:0001-5717.2006.09.004

Wang, Y., Fan, W., Zhang, Y., Peng, T., Chen, X., and Xu, Y. (2006). Kinematics and 40Ar/39Ar Geochronology of the Gaoligong and Chongshan Shear Systems, Western Yunnan, China: Implications for Early Oligocene Tectonic Extrusion of SE Asia. *Tectonophysics* 418 (3-4), 235–254. doi:10.1016/j.tecto.2006.02.005

Wang, Y., Fan, W., Zhang, Y., Peng, T., Chen, X., and Xu, Y. (2006). Kinematics and 40Ar/39Ar Geochronology of the Gaoligong and Chongshan Shear Systems, Western Yunnan, China: Implications for Early Oligocene Tectonic Extrusion of SE Asia. *Tectonophysics* 418, 235–254. doi:10.1016/j.tecto.2006.02.005

Wang, Y., Wang, Y., Schoenbohm, L. M., Zhang, P., Zhang, B., Sobel, E. R., et al. (2020). Cenozoic Exhumation of the Ailaoshan-Red River Shear Zone: New Insights from Low-temperature Thermochronology. *Tectonics* 39, e2020TC006151. doi:10.1029/2020tc006151

Xu, Z., Wang, Q., Cai, Z., Dong, H., Li, H., Chen, X., et al. (2015). Kinematics of the Tengchong Terrane in SE Tibet from the Late Eocene to Early Miocene: Insights from Coeval Mid-crustal Detachments and Strike-Slip Shear Zones. *Tectonophysics* 665, 127–148. doi:10.1016/j.tecto.2015.09.033

Yang, Q., Xu, Y., and Huang, X. (2006). Geochronology and Geochemistry of Granites in the Gaoligong Tectonic belt, Western Yunnan: Tectonic Implications. *Acta Petrologica Sinica* 22, 817. doi:10.3321/j.issn:1000-0569.2006.04.006

Yang, Q., and Xu, Y. (2011). The Emplacement of Granites in Nujiang-Gaoligong belt, Western Yunnan, and Response to the Evolvement of Neo-Tethys. *J. Jilin Univ. (Earth Sci. Edition)* 41, 1353–1361. doi:10.3969/j.issn.1671-5888.2011.05.009

Yang, R., Willett, S. D., and Goren, L. (2015). *In Situ* low-relief Landscape Formation as a Result of River Network Disruption. *Nature* 520, 526–529. doi:10.1038/nature14354

Yao, H., van der Hilst, R. D., and Montagner, J.-P. (2010). Heterogeneity and Anisotropy of the Lithosphere of SE Tibet from Surface Wave Array Tomography. *J. Geophys. Res.* 115, B12307. doi:10.1029/2009JB007142

Yin, A., and Harrison, T. M. (2000). Geologic Evolution of the Himalayan-Tibetan Orogen. *Annu. Rev. Earth Planet. Sci.* 28, 211–280. doi:10.1146/annurev.earth.28.1.211

Zhang, B., Chai, Z., Yin, C. Y., Huang, W. T., Wang, Y., Zhang, J. J., et al. (2017). Intra-continental Transpression and Gneiss Doming in an Obliquely Convergent Regime in SE Asia. *J. Struct. Geology.* 97, 48–70. doi:10.1016/j.jsg.2017.02.010

Zhang, B., Zhang, J., and Zhong, D. (2010). Structure, Kinematics and Ages of Transpression during Strain-Partitioning in the Chongshan Shear Zone, Western Yunnan, China. *J. Struct. Geology.* 32, 445–463. doi:10.1016/j.jsg.2010.02.001

Zhang, B., Zhang, J., Zhong, D., Yang, L., Yue, Y., and Yan, S. (2012). Polystage Deformation of the Gaoligong Metamorphic Zone: Structures, 40Ar/39Ar Mica Ages, and Tectonic Implications. *J. Struct. Geology.* 37, 1–18. doi:10.1016/j.jsg.2012.02.007

Conflict of Interest: The authors declare that the research was conducted in the absence of any commercial or financial relationships that could be construed as a potential conflict of interest.